High-resolution 17–75 keV backlighters for high energy density experiments

H.-S. Park,[1] B. R. Maddox,[1] E. Giraldez,[2] S. P. Hatchett,[1] L. T. Hudson,[3] N. Izumi,[1] M. H. Key,[1] S. Le Pape,[1] A. J. MacKinnon,[1] A. G. MacPhee,[1] P. K. Patel,[1] T. W. Phillips,[1] B. A. Remington,[1] J. F. Seely,[4] R. Tommasini,[1] R. Town,[1] J. Workman,[5] and E. Brambrink[6]

[1]*Lawrence Livermore National Laboratory, Livermore, California 94550, USA*
[2]*General Atomics, San Diego, California 92121, USA*
[3]*NIST, Gaithersburg, Maryland 20899, USA*
[4]*Naval Research Laboratory, Washington, D.C., 20375, USA*
[5]*Los Alamos National Laboratory, Los Alamos, New Mexico 87545, USA*
[6]*Laboratoire pour l'Utilisation des Lasers Intenses, Ecole Polytechnique, 91128 Palaiseau Cedex, France*

(Received 1 May 2008; accepted 24 June 2008; published online 23 July 2008)

17–75 keV one- and two-dimensional high-resolution (<10 μm) radiography has been developed using high-intensity short pulse lasers. High energy $K\alpha$ sources are created by fluorescence from hot electrons interacting in the target material after irradiation by lasers with intensity $I_L > 10^{17}$ W/cm^2. High-resolution point projection one- and two-dimensional radiography has been achieved using microfoil and microwire targets attached to low-Z substrate materials. The microwire size was 10 μm$\times$10 μm$\times$300 μm on a 300 μm$\times$300 μm$\times$5 μm polystyrene substrate. The radiography experiments were performed using the Titan laser at Lawrence Livermore National Laboratory. The results show that the resolution is dominated by the microwire target size and there is very little degradation from the plasma plume, implying that the high-energy x-ray photons are generated mostly within the microwire volume. There are enough $K\alpha$ photons created with a 300 J, 1-ω, 40 ps pulse laser from these small volume targets, and that the signal-to-noise ratio is sufficiently high, for single shot radiography experiments. This unique technique will be used on future high energy density experiments at many new high-power laser facilities. © *2008 American Institute of Physics*. [DOI: 10.1063/1.2957918]

I. INTRODUCTION

Laser driven x-ray sources are used in many applications. Considerable progress has been made in medical imaging where $K\alpha$ sources from the ultrashort pulses are used for angiography[1] and phase-contrast imaging.[2] These experiments radiograph mostly low-Z targets and very often use multiple pulses to accumulate enough photons to acquire adequate signal levels. For inertial confinement fusion (ICF) and high energy density (HED) experiments where most experiments are a single event, the backlighters have to provide enough photons for one shot. Conventional laser-based radiography has traditionally used x-ray emission from thermal plasma sources with moderately high efficiencies. While these sources have been sufficient for previous experiments, a wide range of HED experiments on new laser facilities such as the Omega-Enhanced Performance (EP),[3] the Z-Refurbished (ZR),[4] and the National Ignition Facility (NIF)[5] will require backlighters that can probe high areal density materials with high resolution. For these proposed experiments, efficient higher-energy x-ray sources are required. It has been shown that a significant decrease in the efficiency of traditional thermal sources leads to a limiting x-ray energy near 10 keV.[6] Short pulse nonthermal laser interactions with solid target materials have been demonstrated to produce sufficient x-ray generation above 10 keV for radiography of dense targets.[7,8] Example experiments that require high-energy x-ray radiography include the study of material properties (such as material strength) at very high pressure[9] and mid- to high-Z capsule implosion experiments[10] as depicted in Fig. 1. In a material strength experiment, a sinusoidally rippled sample material is compressed at high pressure and accelerated by a laser plasma–piston drive,[11] such that the rippled surface is hydrodynamically unstable. The ripples grow in amplitude due to the Rayleigh–Taylor (RT) instability, and the material strength retards this growth.[12] The growth rate can be measured by in-flight radiography, and material strength inferred by comparison with two-dimensional (2D) hydrodynamic simulations including a model for high-pressure material strength. In this experiment, the backlighter x-ray energy is dictated by the sample material types and their thicknesses. For aluminum or vanadium samples of $\sim$35 μm thickness, 4.3 or 5.2 keV thermal Heα backlighters are sufficient to obtain high-contrast radiographs of RT growth factors of $\sim$10. On NIF, we plan to study tantalum or other high-Z materials of $\sim$100 μm thickness. In this case, we will need backlighter x-ray energies of $>$40 keV. The second example is radiography of imploding capsules that are made of mid- to high-Z materials. Unlike CH or Be ignition capsules, these mid-Z capsules will have high areal core densities when they are compressed. Again, we will need $>$40 keV backlighters to image spatial features on these targets, which cannot be obtained from traditional thermal x-ray sources.

The $K\alpha$ emission mechanism using high-intensity lasers

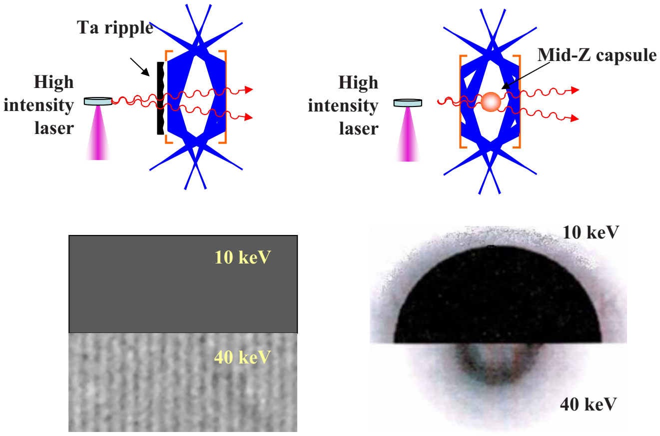

FIG. 1. (Color online) Examples of high-energy-density experiments that require high-energy backlighters on NIF. The left panel is a configuration for a material strength experiment where the ripple growth factors are measured via face-on radiography. The right panel is the mid- to high-Z capsule implosion experiments where capsule implosion symmetry will be studied. The simulated radiography of these targets shows that all require >40 keV radiography due to the high areal density thickness of the samples.

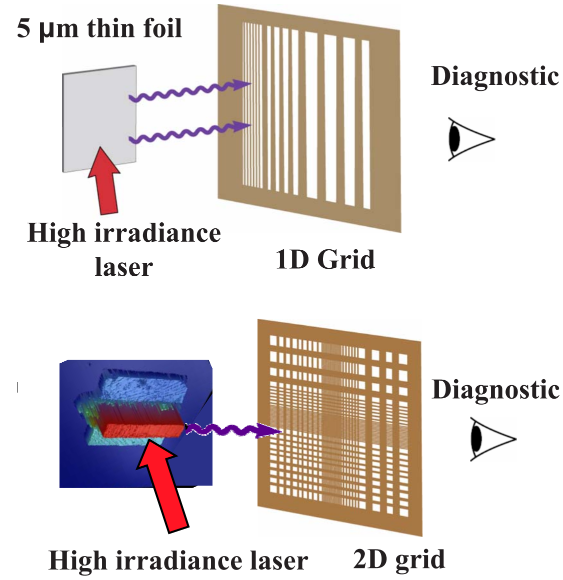

FIG. 2. (Color online) Sketch of point projection radiography using $\sim 5\ \mu m$ thin 1D microfoil sources and $\sim 10\ \mu m \times 10\ \mu m \times 300\ \mu m$ wire microwire source for 2D radiography. For high-energy $K\alpha$ radiography, the x-ray radiation is confined within the fluorescent target material. The small size of the targets produces radiographs with high spatial resolution.

is a promising way of creating 20–100 keV high-energy x rays. When a laser with intensity $>10^{17}$ W/cm^2 strikes a target, a forward directed "spray" of energetic electrons is created, with energies as high as ~ 100 MeV.[13] This forward current draws a return current, and a very strong azimuthal magnetic field is created, with a strength predicted to be 10–100 mega-Gauss or higher. The target also becomes charged, causing all but the most energetic electrons to return for multiple passes through the target ("refluxing").[14] As these energetic electrons traverse the target, bound electrons can be knocked out by electron-electron scattering. If a K-shell electron is knocked out, this inner-shell vacancy is quickly filled by an L-shell or M-shell electron, generating isotropic $K\alpha$ or $K\beta$ radiation.

We have demonstrated that the high-energy x rays generated by high-intensity lasers are created within the high-density bulk part of the target material. High-resolution one dimensional (1D) radiography can therefore be achieved by irradiating a thin microfoil viewed edge-on.[7] As illustrated in Fig. 2, the spatial resolution for this edge-on 1D radiography technique is determined by the microfoil thickness, since the x-ray source generation is confined to the high-density region of the microfoil. Our previous work demonstrated radiography using a 40 keV samarium backlighter that achieved 10 μm spatial resolution. This radiography technique is applied to an integrated experiment that measured the absolute equation of state of aluminum under shock driven condition.[15] In this paper, we present an extension of our 1D radiography work to higher energies of 68 keV, and to 2D using microwires viewed edge-on, as shown in Fig. 2(b).

II. EXPERIMENTAL SETUP

We performed several experiments at the Titan Laser to demonstrate high-energy radiography. Titan uses chirped-pulse amplification,[16] or CPA, to generate short-pulse (1–50 ps), high-power (100 TW) beams. In this CPA system, a short (10–200 fs), low-energy (~ 1 nJ) pulse is generated by a mode-locked oscillator in the front end. This short pulse is stretched in time to ~ 3 ns, then amplified to the 10–300 J level. In the final stage of CPA, the amplified, chirped pulse is temporally compressed back to its original duration. This recompressed pulse is then focused via an off-axis f/3 parabola creating a small laser spot. The small spot size and the short pulse duration create high-intensity beams of 10^{16}–10^{20} W/cm^2. The Titan laser at 1ω (1054 nm) can deliver 150 J for 1 ps and 300 J for 40 ps. During our experiments, we varied the laser energy between 30 and 300 J with pulse durations between 0.5 and 40 ps.

We measured the laser spot size at low power using a microscope lens coupled to a charge coupled device (CCD) camera. This measurement method may be of limited accuracy because of B integral and main amplifier pump-induced effects; however, they provide a qualitative measure of spot sizes as a function of parabola focusing. Figure 3(a) shows the beam images displayed in log scale. Since most of our experiments are performed either at the best focus or 300 μm further upstream toward the focusing parabola, we characterized the laser beam spots at these locations. Without adaptive optics, the laser spot has multiple lobes when it is defocused. Assuming the brightest pixel is the center of the laser spot, the pixel intensity as a function of distance is plotted in Figs. 3(b) and 3(c), which shows the cumulative laser energy fraction. We observe that 50% of the laser energy is contained within a 14 μm radius at the best focus and a 54 μm radius when defocused. In both cases, the entire laser energy is completely contained within our typical foil size of 300 $\mu m \times 300\ \mu m$. We use the defocused setting for many of our experiments in order to reduce the bremsstrahlung background that increases as the laser intensity increases while optimizing $K\alpha$ yield, which is measured to be fairly independent of laser intensity between 10^{17} and

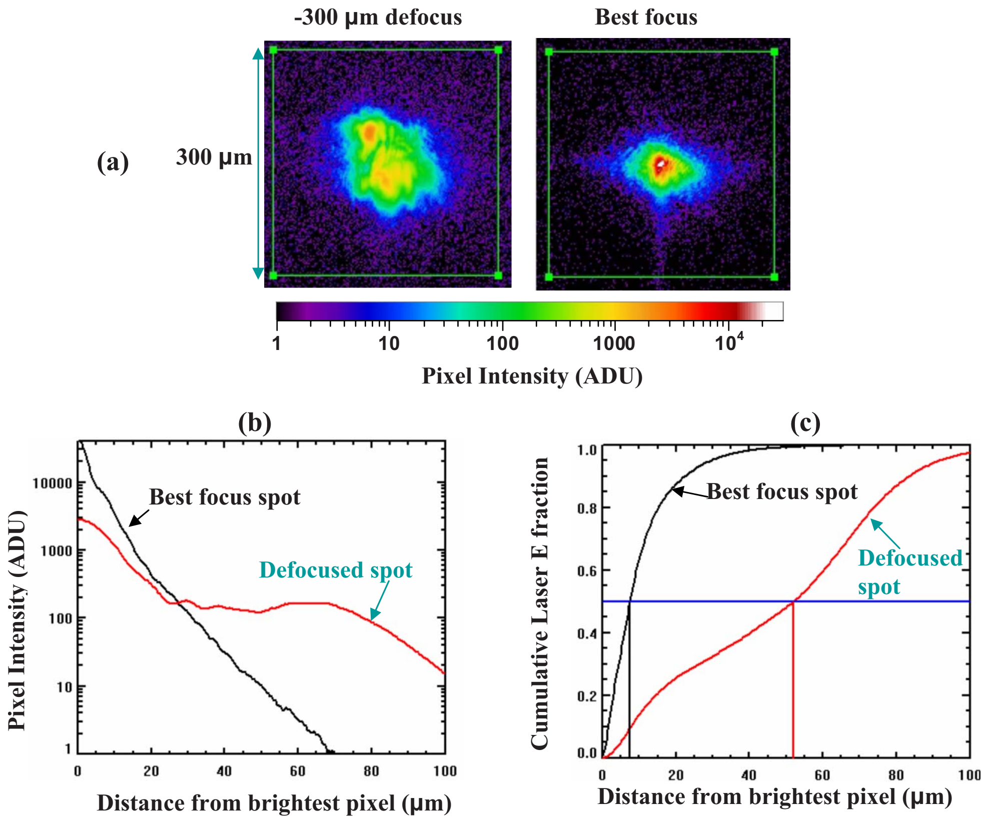

FIG. 3. (Color online) Laser spot image at its best focus and in a defocused condition where the target is placed 300 μm toward the parabola. 50% of the laser energy is contained within a 14 μm radius at the best focus and within a 54 μm radius for the defocused case.

10^{19} W/cm^2.[7] A schematic of the Titan experiment is given in Fig. 4. The microflag or microwire radiography targets were placed at the focal spot and rotated precisely to give an edge-on view to the imaging detectors at two locations.

III. DETECTORS

For high-energy x-ray imaging, we use point projection onto either image plates and or a Gd_2O_2S scintillator backed by a Roper Scientific CCD camera. In this setup, the angle between the incident backlighter laser and the detector was 16 degrees for the Gd_2O_2S/CCD detector and 40.7 degrees for the image plate detector.

Image Plate Detector. Image plates detect incoming x-ray photons on a uniform layer of small grain BaFBrI:Eu^{2+} crystals.[17] Excited electrons are trapped by empty halogen ion sites in the crystal, making metastable color centers capable of emitting radiation. Irradiation by a laser beam absorbed by the color centers excites the electrons again, which quickly recombine with holes, and the recombination energy is transferred to the Eu ions, resulting in photostimulated luminescence (PSL). For our experiment, we use the BAS-SR type image plates manufactured by Fujifilm.[18]

Gd_2O_2S/CCD *Detector.* The other detector was a terbium-doped gadolinium oxysulfide (Gd_2O_2S:Tb) phosphor screen coupled to a front-illuminated CCD via a 1:1 fiber optic face plate. The phosphor converts incoming x rays into ~550 nm optical photons that are collected by the CCD detector. The CCD has 2048 pixels $\times$ 2048 pixels each 24 μm $\times$ 24 μm. This camera is manufactured by Roper Scientific Inc.

Single-photon counting camera. In addition to the detectors used in point projection imaging, we also used two different types of spectrometers. The first was a single-photon counting camera. This is a CCD camera that absorbs the x-ray photons directly in the silicon depletion region. When an x-ray photon is fully absorbed within a pixel, photoelectrons are created. For a silicon CCD, the pair creation energy

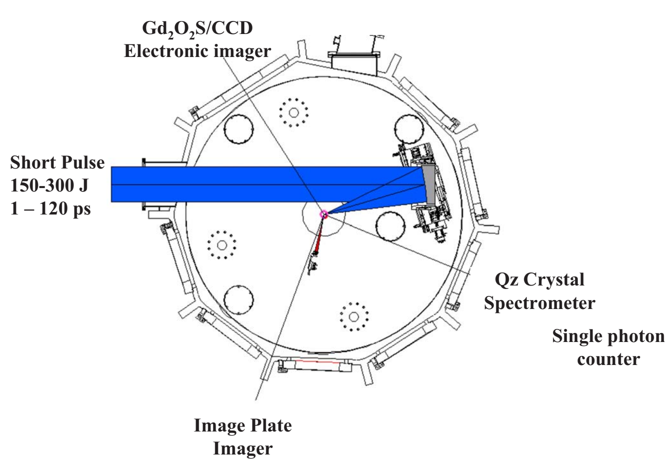

FIG. 4. (Color online) Titan experimental setup. Two different types of imaging devices (Image Plate and Gd_2O_2S/CCD imagers) and two different spectrometers (single-photon counting camera and curved Qz crystal spectrometer) were employed to measure spatial resolution and $K\alpha$ conversion efficiencies.

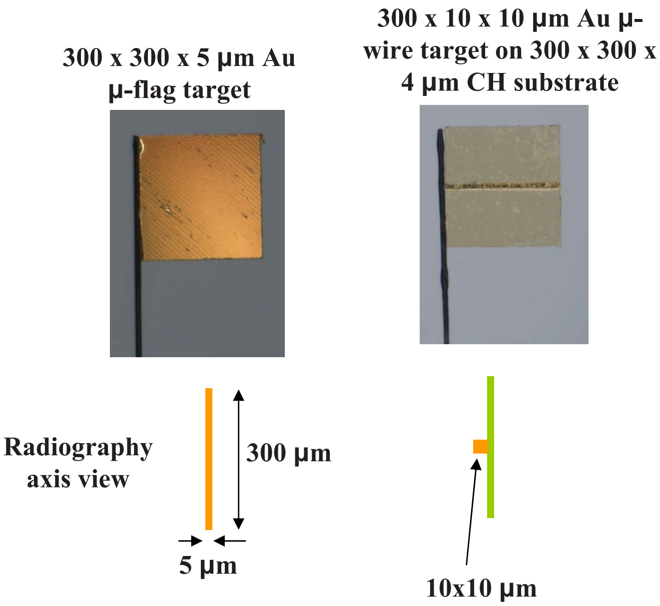

FIG. 5. (Color online) Fabricated microfoil and microwire targets. These are examples used for Au $K\alpha$ radiography. We have tested Mo, Ag, and Sm targets that are fabricated with similar geometries. The radiographs are taken along an axis providing an edge-on view of the microwire or micro dot.

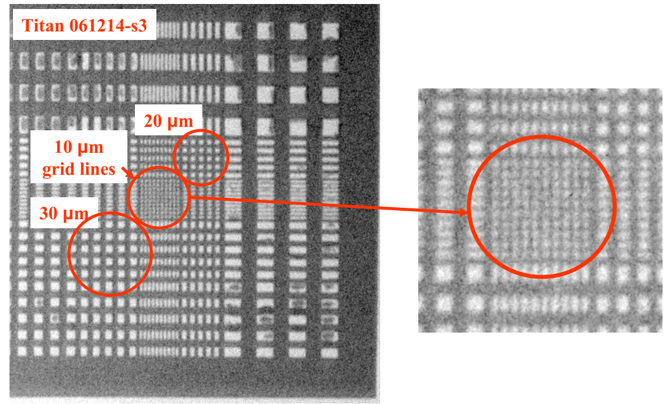

FIG. 6. (Color online) The results of Ag $K\alpha$ radiography with microwire target. The diagonal sections with 10, 20, and 30 μm grids are denoted. The central 10 μm grid region is well resolved.

is 3.65 eV at room temperature; a 1 keV x-ray photon, if absorbed completely in one pixel, will produce 274 photoelectrons. The number of photoelectrons collected on a pixel, then, is proportional to the incoming x-ray energy. Because of the fairly thin (16 μm) depletion layer of readily available CCDs, this detector is sensitive only up to x-ray energies of ~30keV.[19,20]

Quartz crystal spectrometer. The second spectrometer employed a transmission crystal in Laué geometry. This instrument uses a Qz(10-11) crystal curved to a radius of 254 mm.[21] The curvature of the quartz crystal focuses photons that are registered on an image plate located 254 mm behind the crystal. With this spectrometer we were able to record spectra up to 80 keV with a spectral resolution of 150.

IV. LASER TARGET

For radiography diagnostic development, we made microfoil and microwire targets mounted on top of low-Z substrates to create small point sources for 1D and 2D radiography. Figure 5 shows an example of an Au microfoil and a Au microwire target. These targets were fabricated by General Atomics. The microfoil is a simple 300 μm $\times$ 300 μm $\times$ 5 μm Au foil held by a 6 μm diameter carbon fiber. The edge of this foil is cleanly sheared so that very little slag is seen from the edge-on view. Similar targets, made of Mo, Ag, and Sm, have also been tested in our experiments.

The microwire target was difficult to fabricate. The $K\alpha$ radiator material (here, Au) was deposited on top of the approximately 4–5 μm thin CH substrate; then micromachined into a small wirelike volume. We chose CH as the substrate in order to reduce the bremsstrahlung background that scales as $\sim Z^2$. We chose the micromachining process (instead of gluing a wire onto the substrate) so that the microwire had better contact with the substrate. The short pulse laser hits the microwire side-on. The laser spot sizes are bigger (as discussed in Sec. II) than the microwire size; the laser energy that misses the wire is intercepted by the substrate. The substrate plays the role of generating more refluxing hot electrons that may impact the fluorescent material, generating more $K\alpha$ x rays.

V. RADIOGRAPHY RESULTS

A. 22 keV 2D radiography with a microwire target

In order to demonstrate 2D radiography, we fabricated a test pattern consisting of an orthogonal stack of 1D slits (10, 20, 30, 40, and 80 μm) on a 25 μm thick Au substrate. This test pattern was fabricated by a mask projection technique using an Excimer laser.[22]

Using this pattern, we tested the performance of a 2D radiography Ag microwire target that produces 22 keV x rays containing both $K\alpha$ and the bremsstrahlung x rays in this energy band. The expected source spectrum is quasimonochromatic as the source is filtered by the K edge of the Ag filter. The laser energy for this shot was 242 J with a 40 ps pulse duration. We defocused the laser to have 50% of laser energy contained within a 54 μm radius area. The resulting radiograph is shown in Fig. 6. The diagonal sections with 10, 20, and 30 μm grids are denoted in the figure. (For example, by a 10 μm grid, we mean that the wire widths are 10 μm, and the period or distance between adjacent wires is 20 μm.) With a 10 μm source size, we expected to resolve no better than 10 μm features as seen in this image. This image is taken with the Gd_2O_2S/CCD detector with an imaging magnification of 17.

We further analyzed this image to obtain the point spread function. We first created an ideal grid image by differentiating in the vertical and horizontal directions the image of a small, 30 μm grid section. This ideal grid image was smeared by a 2D Gaussian resolution function, $R(r) = \exp[-(r^2/2\ \sigma^2]$, and σ was varied until the smeared ideal grid most closely resembled the experimental image, as shown in Fig. 7(a). Figure 7(b) shows the horizontal and vertical line-outs from the central section of the experimental image versus the best-fit convoluted grid image. They match

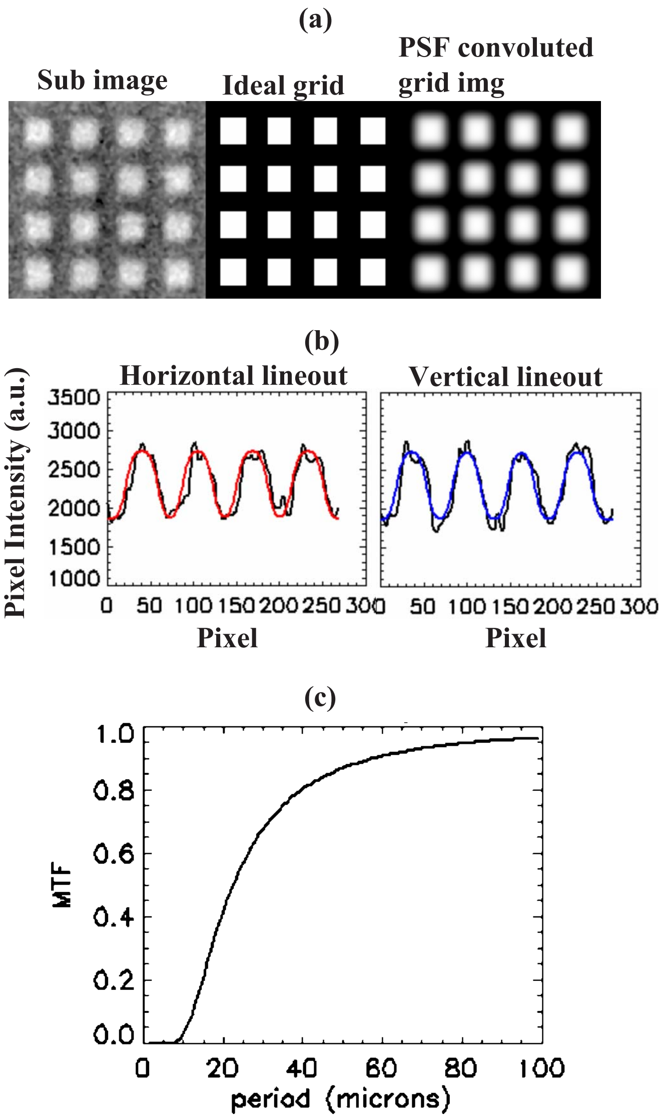

FIG. 7. (Color online) MTF analysis of the radiographs in Fig. 5. The point spread function is obtained by finding the best match of the data with an ideal grid image convoluted with the point spread function. We obtain an ~40% MTF for 20 μm periods with the 250 J Titan laser. Improved MTFs are expected with higher-energy lasers.

well implying that the fitted image reproduces the data quantitatively. The resulting fit gave σ=4.2 μm, corresponding to a full width at half-maximum (FWHM) resolution of $2(2\ \ln 2)^{1/2}\sigma$=9.9 μm. This is consistent with the microwire size of 10 μm and proves that the high-energy x-ray photons come mainly from the microwire bulk region and that the spatial resolution is limited by the microwire size. The Fourier transform of the resolution function gives the modulation transfer function (MTF), the result of which is

$$M(k) = e^{-(k\sigma)^2/2}, \quad \text{where } k = \frac{2\pi}{\lambda}.$$

Here $M(k)$ is the MTF, σ is the above fit point spread function parameter, and λ is the period of the modulation. The resulting $M(k)$ is plotted in Fig. 7(c). From this plot we deduce that we can achieve a 40% MTF for 20 μm spatial features. This experiment was conducted with a laser energy

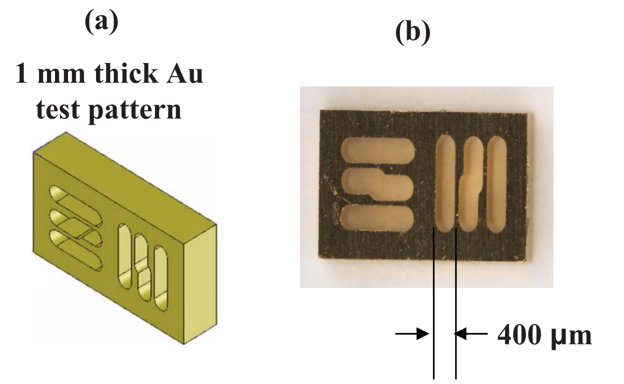

FIG. 8. (Color online) Test target for Au radiography (68 keV). The target is made of 1 mm thick Au material with edges machined using EDM.

of ~250 J. The MTF is expected to be higher with a higher energy laser, due to the higher signal in the experimental images.

B. 68 keV 1D and 2D radiography spatial resolutions with microfoils and microwire targets

We have also tested Au $K\alpha$ backlighter targets for 68 keV radiography in the microfoil and microwire geometries. For 68 keV radiography, the Au grid test pattern (25 μm thick Au substrate) used to test radiography at 22 keV was inadequate as the attenuation length of Au at 68 keV is 163 μm. Instead, we measured the resolution using 1 mm thick Au plates that had several channels carved all the way through by EDM (Electrical Discharge Machining). The edges of the channels served as knife-edge targets for testing the resolution, and the EDM process minimized any slag that could be seen when viewed edge-on (Fig. 8).

Two radiographs from these experiments are shown in Fig. 9. The laser parameters used for these shots were similar to the settings used for the 22 keV Ag radiography described above. Fuji BAS-SR type image plates were used to record these images. The image in Fig. 9(a) was taken with a 1D microflag target positioned in the vertical plane, perpendicular to the image. The 1D nature of the spatial resolution is

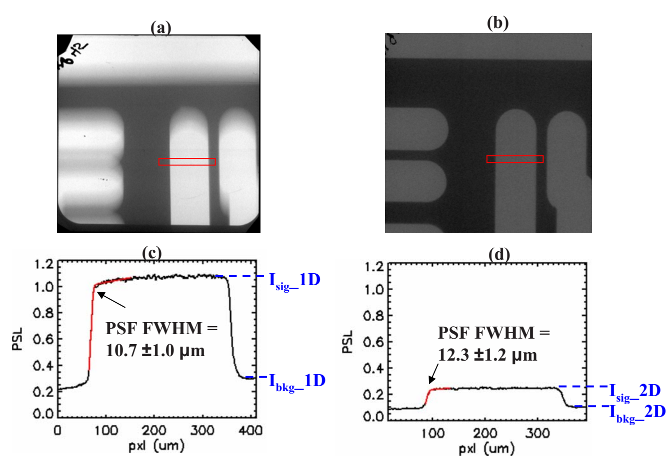

FIG. 9. (Color online) Radiography results from the Au microflag and microwire targets. The 1D and 2D nature of the images are clear. The edges were fit to an edge spread function (see text).

clear; the spatial resolution is good only in the horizontal direction and only near the center of the image where the image plate sees only the edge of the Au test target because of its thickness. The image in Fig. 9(b) was taken with a microwire target pointed at the image plate. Unlike the microfoil target, this image shows good spatial resolution in all directions. To quantify the spatial resolution, we fit line-outs across the edges [Fig. 9(b)] to an edge spread function (ESF). The ESF is the integral response function of a Gaussian point spread function (PSF) which fits our knife-edge data well when combined with a linear background term,

$$\mathrm{ESF} = I_0 \cdot \mathrm{erf}\left(\frac{x}{\sigma}\right) + a_0 + a_1 x,$$

where

$$\mathrm{erf}\left(\frac{x}{\sigma}\right) = \frac{2}{\pi}\int_0^{x/\sigma} e^{-t^2} dt$$

$$I_0, \sigma, a_0, a_1 = \text{fitting coefficients}.$$

The fit results are shown as red lines in Figs. 9(c) and 9(d). From this fit, we find the FWHM of the PSF to be 10.7 ± 1.0 μm in the 1D image and 12.3 ± 1.2 μm in the 2D image, respectively. These measured numbers are larger than the actual foil thickness of 5 μm and wire size of 10 μm. This is likely caused by alignment errors of the thick test pattern target. After taking our 0.5 degree alignment accuracy into account, the resulting FWHM is consistent with the physical thickness of the microfoil.

In this direct comparison of microfoil and microwire radiography, it is clear that the $K\alpha$ emission is confined to the bulk fluorescent material and any plasma blow-off or substrate emission does little to degrade the spatial resolution.

C. Radiometric intensities of microflag and microwire sources

The differences in relative photon output between the microflag and microwire targets were apparent in these experiments. The images are presented in PSL units that linearize the image plate scanner output digital scale. We denote the signal levels in the line-outs by $I_{\mathrm{sig_}}$1D and $I_{\mathrm{sig_}}$2D and the background levels by $I_{\mathrm{bkg_}}$1D and $I_{\mathrm{bkg_}}$2D. We measure $I_{\mathrm{sig\_}}1\mathrm{D}=1.08 \pm 0.03$, $I_{\mathrm{bkg\_}}1\mathrm{D}=0.21 \pm 0.15$, $I_{\mathrm{sig\_}}2\mathrm{D}=0.25 \pm 0.018$, and $I_{\mathrm{bkg\_}}2\mathrm{D}=0.088 \pm 0.011$. From these numbers, we calculate that the number of x-ray photons emitted by the source and captured by the image plates by $(I_{\mathrm{sig\_}}1\mathrm{D}\text{-}I_{\mathrm{bkg\_}}1\mathrm{D})/(I_{\mathrm{sig\_}}2\mathrm{D}\text{-}I_{\mathrm{bkg\_}}2\mathrm{D})$. The resulting ratio is 5.4 ± 1.2.

The radiography signal level difference ($I_{\mathrm{sig_}}$1D versus $I_{\mathrm{sig_}}$2D) may be explained by the size of the area on the fluorescent intersected by the laser. For the microflag target, 100% of the laser energy struck the Au material whereas for the microwire only 25% of the laser energy struck the Au as we operated the laser in "defocused" mode for these shots. As discussed in Sec. II, the defocused laser spot has a radius of 54 μm. If the laser spot is Gaussian, the intersection with a 10 μm diameter wire is only 25% of the total beam area.

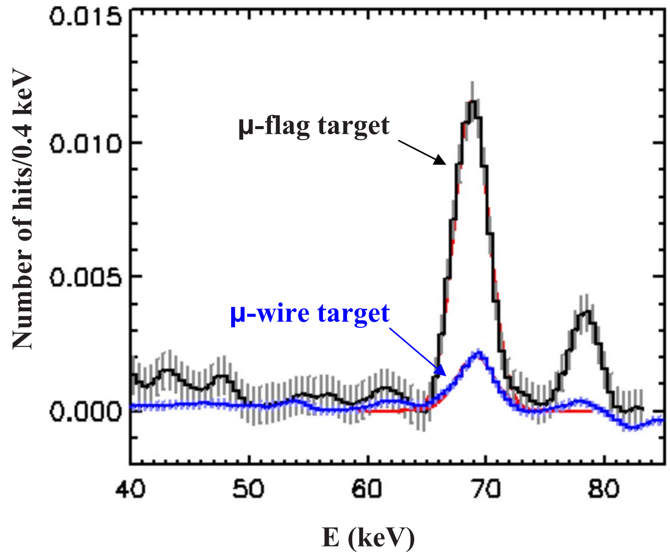

FIG. 10. (Color online) Difference in $K\alpha$ yield between microflag and microwire targets measured by the Qz crystal spectrometer. The histograms are continuum background subtracted. After accounting for the difference in laser energy, the ratio in the $K\alpha$ yield between these two types of targets is 5.2 ± 1.5.

We observe a similar radiometric difference in the signal level between the 1D microflag targets and the 2D microwire targets in the $K\alpha$ yield. In Fig. 10, we compare microflag and microwire Au target $K\alpha$ spectra measured by the Qz spectrometer. The targets are identical to the ones used in the radiography testing. The laser energy was 280 J and we used the slightly defocused laser spot (σ=12 μm) to irradiate the microwire. In the figure, the spectral histogram is continuum background subtracted; the statistical error on each data point is deduced from the fluctuations in the background area and shown in gray bars; the red dotted line is the Gaussian fitting of the $K\alpha$ peak region. The $K\alpha$ yield is defined to be the integrated area in the peak region. After correcting shot-to-shot differences in the laser energy, our measurements indicate that the $K\alpha$ yield ratio between the microflag target and the microwire target is 5.2 ± 1.5. The major source of the error is from the background subtracting method because the measured signal for the microwire was small compared to the signal of microflag. This is consistent with the measurement of radiometric data indicating the radiography is little contaminated by the bremsstrahlung background. More systematic studies on laser intensity dependency, laser spot variations, and other laser parameters will be performed in future.

VI. $K\alpha$ CONVERSION EFFICIENCIES FOR MICROFOIL TARGETS

We have determined $K\alpha$ conversion efficiencies as a function of target material up to the Pb $K\alpha$ line of 75 keV. In these measurements, the targets were 0.5 mm $\times$ 4 mm $\times$ 25 μm thick in size. The laser parameters were 40 ps at 220 J with a focal spot of $\sim$54 μm in diameter yielding a laser intensity of 2×10^{17} W/cm^2.

For this experiment, we measured the efficiency of converting laser energy to $K\alpha$ x rays using two different spec-

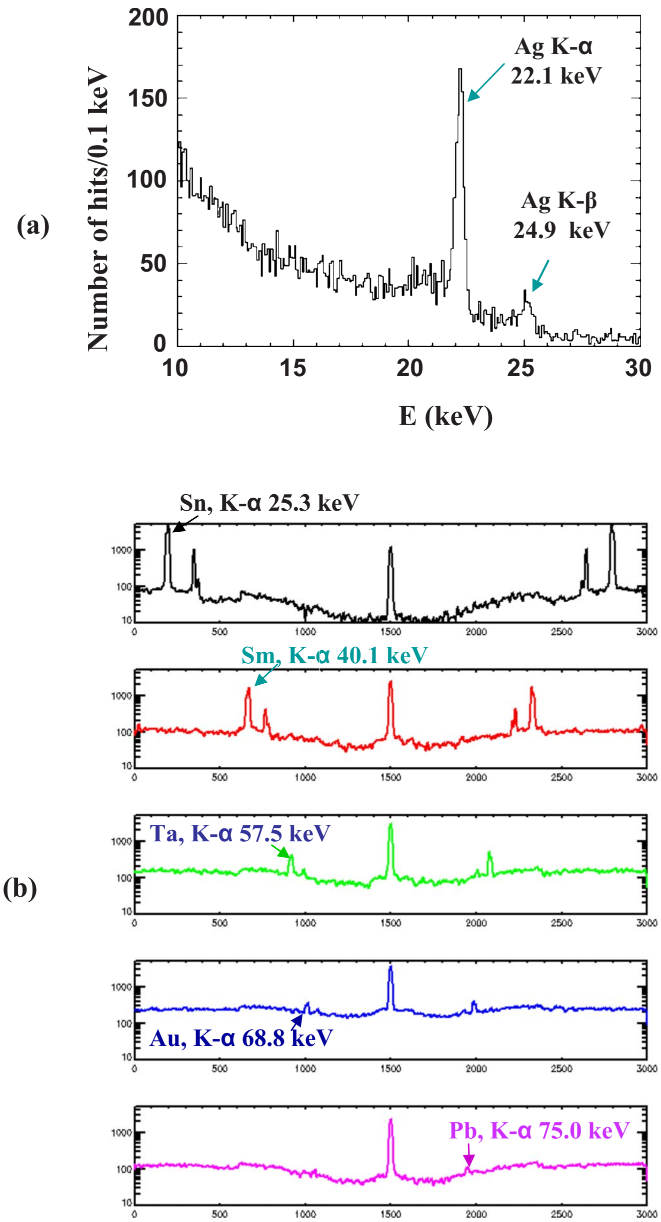

FIG. 11. (Color online) $K\alpha$ yield measurements using the single-photon counting camera (a) and the curved Qz crystal spectrometer (b) for various target materials. We measure absolute $K\alpha$ conversion efficiencies using the single-photon counting camera at 8–25 keV and relative conversion efficiencies using Qz spectrometer at 20–80 keV. By normalizing the $K\alpha$ conversion efficiencies at 22 keV, we measure the absolute $K\alpha$ efficiencies from 17–75 keV.

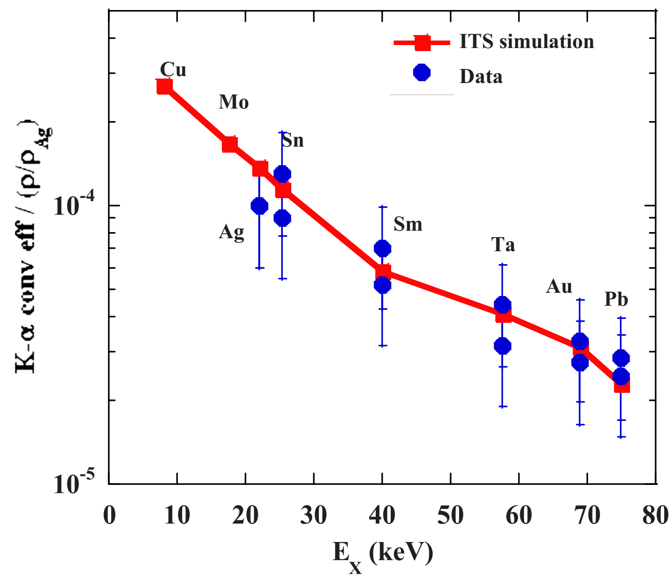

FIG. 12. (Color online) Measurements of the $K\alpha$ conversion efficiency of different target materials. The two different data points correspond to the two different measurements of the same target types. The ITS Monte Carlo simulation is plotted as the solid line.

trometers: The single photon counting (SPC) CCD camera for $K\alpha$ energies between 10 and 30 keV, and the quartz crystal spectrometer for $K\alpha$ energies between 15 and 78 keV. Details of these detectors were given in Sec. II. Figure 11(a) shows an example of the spectrum from a Ag microwire target measured by the SPC detector. The $K\alpha$ and $K\beta$ peaks are clearly visible. We count the number of hits above the background in the $K\alpha$ and $K\beta$ peaks and multiply by the photon energy to obtain $E_{K\text{-}\alpha}$(measured), the measured amount of $K\alpha$ or $K\beta$ radiation in the detector. The conversion efficiency is then calculated by

$$\varepsilon_{\text{conv}} = \frac{E_{K\alpha}}{E_{\text{laser}}} \cdot \frac{1}{\varepsilon_{\text{detector}} \cdot \varepsilon_{\text{single\_hit}} \cdot T_{\text{filter}}} \cdot \frac{4\pi}{\Omega_{\text{detector}}},$$

where $\varepsilon_{\text{conv}}$ is the conversion efficiency, $\varepsilon_{\text{detector}}$ is detector quantum efficiency, $\varepsilon_{\text{single\_hit}}$ is the probability that all of the 22 keV energy from a single photon is captured in one pixel, T_{filter} is the transmission factor through the filter materials, and Ω_{detector} is the detector solid angle. The detection efficiency for the SPC is absolutely calibrated using a Cd109 radioactive source.[23] The calibration allows us to determine the combined efficiency $\varepsilon_{\text{detector}} \times \varepsilon_{\text{single\_hit}}$ to be $(6.24 \pm 0.93)\%$ for Fe 55, $(1.47 \pm 0.22)\%$ for Cu $K\alpha$, and $(0.134 \pm 0.02)\%$ for Ag $K\alpha$. Knowing these efficiencies allows us to measure the absolute conversion efficiencies for Cu, Mo, Ag, and Sn targets with this detector. Details on these single-photon counting camera efficiencies will be published.[24]

For the higher Z target materials, we used the crystal spectrometer as described in Ref. 25. Figure 11(b) shows data for Sn, Sm, Ta, Au, and Pb target materials. Again we count the number of hits above the background. The detector (image plate) response is calculated assuming that the BaFBrI:Eu^{2+} phosphor material is 121 μm thick with a density of 3.07 g/cm^3, then using the standard energy-dependent x-ray absorption coefficients for this material. The Qz crystal response is calculated using the XOP simulation code for a Laué geometry.[26] This procedure gives only a relative response function for the crystal spectrometer. Since both the crystal spectrometer and the SPC can measure Ag $K\alpha$ photons, the relative responses of the crystal spectrometer were scaled so that the measurement of the Ag $K\alpha$ made by the two instruments agreed. This provided an absolute calibration of the crystal spectrometer for the other measurements. The resulting conversion efficiencies divided by the ratio of the material density to the Ag density are plotted in Fig. 12.

The two different data points correspond to the two different shots of the same target types. Each set of the data was taken within a day in order to minimize the systematic changes such as laser power condition and target setup configuration. The errors (40%) on these measurements are from the statistical error of the $K\alpha$ peak counts, the error on the single photon counting camera detection efficiency (15%), the error on the detector efficiency (20%,), the uncertainty in the crystal spectrometer efficiency (20%), and the average shot-to-shot variance (23%).

While there are a few analytical models of femtosecond $K\alpha$ x-ray generation,[27] we compare these results with Monte Carlo (MC) simulations using the ITS (Integrated Tiger Series) code.[28] The MC simulation of $K\alpha$ x-ray production proceeds in two steps. First, a hot-electron temperature is determined from the formula[29]

$$T_{\mathrm{hot}} = \left(\frac{I \cdot \lambda^2}{10^{19} \dfrac{W}{cm^2} \cdot \mu m^2} \right)^{1/3} \cdot MeV,$$

where I is the laser intensity in $\mathrm{W/cm^2}$ and λ is the laser wavelength in μm. Electrons are generated having energies taken from the Boltzmann distribution characteristic energy. Each electron is then transported through the target material using the ITS Monte Carlo code. In the calculation, the electrons are injected at the surface of the solid target into a cone of half-angle 26° into the target. The ITS simulation determines the number of $K\alpha$ x-ray photons per hot electron per steradian as a function of angle. The number of hot electrons as a function of laser intensity is determined by the formula

$$\varepsilon_{\mathrm{hotelectrons}} = 0.096 \cdot \left(\frac{I}{10^{18} \dfrac{W}{\mathrm{cm}^2}} \right)^{0.29},$$

where I is the laser intensity in $\mathrm{W/cm^2}$. This equation is derived from experimental measurements by Yasuike *et al.*[30]. By multiplying the yield of $K\beta$ photons per electron per steradian from the first step by the number of hot electrons from the second step, we obtain the $K\alpha$ yield per steradian.

The resulting output of the MC simulations is noted as the red line in Fig. 12. The current simulation set does not account for electron refluxing,[31] which can increase $K\alpha$ production. Note that we have normalized the simulated conversion efficiencies so that it agrees with the measured Ag $K\alpha$ data by multiplying each point on the curve by a constant correction factor of 2. This correction factor may be accounted for by electron refluxing in our target.

VII. CONCLUSION

We have obtained high-resolution, high-energy radiographs using a high-intensity laser focused onto microflag and microwire targets. We find that the high-energy $K\alpha$ photon emission is confined to the target volume resulting in a spatial resolution in the images defined by the fluorescent material size. When viewed edge-on and using 5–10 μm microwire and microflag targets, we obtained spatial resolutions of ~10 μm FWHM. We find that the $K\alpha$ conversion efficiencies for the microwire targets are a factor of 10 lower than for the microflag targets. However, in practical radiography experiments, some fraction of the non-$K\alpha$ bremsstrahlung photons having energies around the $K\alpha$ energy contribute to the number of photons collected increasing the signal level by a factor of 2. Finally, we measured $K\alpha$ conversion efficiencies up to the 75 keV Pb $K\alpha$ line; the results are compared to the Monte Carlo (ITS) simulations with reasonable agreement. At 75 keV, the $K\alpha$ conversion efficiency, 2.5×10^{-5}, is four times lower than the conversion efficiency at the 22 keV Ag $K\alpha$ line.

[1] E. Andersson, G. Hölzer, E. Förster, M. Grätz, L. Kiernan, A. Sjögren, and S. Svanberg, J. Appl. Phys. **90**, 3048 (2001).

[2] R. Toth, S. Foumaux, T. Ozaki, M. Servol, and J. C. Keiffer, Phys. Plasmas **14**, 053506 (2006).

[3] L. J. Waxer, D. N. Maywar, J. H. Kelly, T. J. Kessler, B. E. Kruschwitz, S. J. Loucks, R. L. McCrory, D. D. Meyerhofer, S. F. B. Morse, C. Stoeckl, and J. D. Zeugel, Opt. Photonics News **16**, 30 (2005).

[4] D. H. McDaniel, M. G. Mazarakis, D. E. Bliss, J. M. Elizondo, H. C. Harjes, H. C. Ivis III, D. L. Kitterman, J. E. Maenchen, T. D. Pointon, S. E. Rosenthal, D. L. Smith, K. W. Struve, W. A. Stygar, E. A. Weinbrecht, D. L. Johnson, and J. P. Corley, AIP Conf. Proc. **651**, 23 (2002).

[5] J. A. Paisner, E. M. Campbell, and W. J. Hogan, Fusion Technol. **26**, 755 (1994).

[6] J. Workman and G. A. Kyrala, Proc. SPIE **4504**, 168 (2001).

[7] H. S. Park, D. M. Chambers, H.-K. Chung, R. J. Clarke, R. Eagleton, E. Giraldez, T. Goldsack, R. Heathcote, N. Izumi, M. H. Key, J. A. King, J. A. Koch, O. L. Landen, A. Nikroo, P. K. Patel, D. F. Price, B. A. Remington, H. F. Robey, R. A. Snavely, D. A. Steinman, R. B. Stephens, C. Stoeckl, M. Storm, M. Tabak, W. Theobald, R. P. J. Town, J. E. Wickersham, and B. B. Zang, Phys. Plasmas **13**, 056309 (2006).

[8] L. M. Chen, P. Forget, R. Toth, J. C. Kieffer, A. Krol, C. C. Chamberlain, B. X. Hou, J. Nees, and G. Mourou, Proc. SPIE **5030**, 923 (2003).

[9] B. A. Remington, G. Bazan, J. Belrak, E. Bringa, M. Caturla, J. D. Colvin, M. J. Edwards, S. G. Glendinning, D. S. Ivanonv, B. Kad, D. H. Kalantar, M. Kumar, B. F. Lasinski, K. T. Lorenz, J. M. McNaney, D. D. Meyerhofer, M. A. Meyers, S. M. Pollaine, D. Rowley, M. Schneider, J. S. Stölken, J. S. Wark, S. V. Weber, W. G. Wolfer, B. Yaakobi, and L. V. Zhigiley, Metall. Mater. Trans. A **35A**, 2587 (2004); B. A. Remington, P. Allen, E. M. Bringa, J. Hawreliak, D. Ho, K. T. Lorenz, H. Lorenzana, J. M. McNaney, M. A. Meyers, S. W. Pollaine, K. Rosolankova, B. Sadik, M. S. Schneider, D. Swift, J. Wark, and B. Yaakobi, Mat. Sci. Technol. **22**, 474 (2006).

[10] T. R. Dittrich, S. W. Haan, M. M. Marinak, S. M. Pollaine, D. E. Hinkel, D. H. Munro, C. P. Verdon, G. L. Strobel, R. McEachern, R. C. Cook, C. C. Roberts, D. C. Wilson, P. A. Bradley, L. R. Foreman, and W. S. Varnum, Phys. Plasmas **6**, 2164 (1999).

[11] J. Edwards, K. T. Lorenz, B. A. Remington, S. Pollaine, J. Colvin, D. Braun, B. F. Lasinski, D. Reisman, J. M. McNaney, G. A. Greenough, R. Wallace, H. Louis, and D. Kalantar, Phys. Rev. Lett. **92**, 075002 (2004).

[12] K. T. Lorenz, M. J. Edwards, S. G. Glendinning, A. F. Jankowski, J. McNaney, S. Pollaine, and B. A. Remington, Phys. Plasmas **12**, 056309 (2005).

[13] M. H. Key, M. D. Cable, T. E. Cowan, K. G. Estabrook, B. A. Hammel, S. P. Hatchett, E. A. Henry, D. E. Hinkel, J. D. Kilkenny, J. A. Koch, W. L. Kruer, A. B. Langdon, B. F. Lasinski, R. W. Lee, B. J. MacGowan, A. MacKinnon, J. D. Moody, J. J. Moran, A. A. Offenberger, D. M. Pennington, M. D. Perry, T. H. Phillips, T. C. Sangster, M. S. Singh, M. A. Stoyer, M. Tabak, G. L. Tietbohl, M. Tsukamoto, K. Wharton, and S. C. Wilks, Phys. Plasmas **5**, 1966 (1998).

[14] Y. Sentoku, K. Mima, P. Kaw, and K. Nishikawa, Phys. Rev. Lett. **90**, 155001 (2003).

[15] A. Benuzzi-Mounaix, M. Koenig, A. Ravasio, T. Vinci, N. Ozaki, M. Rabec le Gloahec, B. Loupias, G. Huser, E. Henry, S. Bouquet, C. Michaut, D. Hicks, A. MacKinnon, P. Patel, H. S. Park, S. Le Pape, T. Boehly, M. Borghesi, C. Cecchetti, M. Notley, R. Clark, S. Bandyopadhyay, S. Atzeni, A. Schiavi, Y. Aglitskiy, A. Faenov, T. Pikuz, D. Batani, R. Dezulian, and K. Tanaka, Plasma Phys. Controlled Fusion **48**, B347 (2006).

[16] D. Strickland and G. Mourou, Opt. Commun. **56**, 219 (1985).

[17]M. Sonoda, M. Takano, J. Miyahara, and H. Kato, Radiology **148**, 833 (1983).
[18]Certain commercial equipment, instruments, or materials are identified in this paper in order to specify the experimental procedure adequately. Such identification is not intended to imply recommendation or endorsement by the U.S. government, nor is it intended to imply that the materials or equipment identified are necessarily the best available for the purpose.
[19]M. Nishiuchi, K. Koyama, T. Tsuru, H. Awaki, H. Tomida, and K. Hamaguchi, Proc. SPIE **3445**, 268 (1998).
[20]H. S. Park, N. Izumi, M. H. Key, J. A. Koch, O. L. Landen, P. K. Patel, T. W. Phillips, and B. B. Zhang, Rev. Sci. Instrum. **75**, 4048 (2004).
[21]J. F. Seely, G. E. Holland, L. T. Hudson, C. I. Szabo, A. Henins, H. S. Park, P. K. Patel, R. Tommasini, and J. M. Laming, High Energy Density Phys. **3**, 263 (2007).
[22]G. Ogura and R. Hack, Med. Device Diagn. Ind. **3**, 124 (2006).
[23]H. S. Park, J. A. Koch, O. L. Landen, T. W. Phillips, T. J. Goldsack, E. Clark, R. Eagleton, and R. D. Edwards, Proc. SPIE **5196**, 213 (2004).
[24]B. R. Maddox, H. S. Park, B. A. Remington, and M. A. McKernan, "Calibration and characterization of single photon counting cameras for short-pulse laser experiments," Rev. Sci. Instrum. (submitted).
[25]R. Tommasini, H. S. Park, P. Patel, B. Maddox, S. Le Pape, S. P. Hatchett, B. A. Remington, M. H. Key, N. Izumi, M. Tabak, J. A. Koch, O. L. Landen, D. Hey, and A. MacKinnon, AIP Conf. Proc. **926**, 248 (2007).
[26]M. Sanchez del Reio and R. J. Dejus, Proc. SPIE **3152**, 148 (1997).
[27]D. Salzmann, Ch. Reich, I. Uschmann, and E. Förster, Phys. Rev. E **65**, 036402 (2002).
[28]J. A. Halbleib, R. P. Kensek, and G. D. Valdez, IEEE Trans. Nucl. Sci. **39**, 1025 (1992).
[29]F. N. Beg, A. R. Bell, A. E. Dangor, C. N. Danson, A. P. Fews, M. E. Glinsky, B. A. Hammel, P. Lee, P. A. Norreys, and M. Tatarakis, Phys. Plasmas **4**, 447 (1997).
[30]K. Yasuike, M. H. Key, S. P. Hatchett, R. A. Snavely, and K. B. Wharton, Rev. Sci. Instrum. **72**, 1236 (2001).
[31]J. Myatt, W. Theobald, J. A. Delettrez, C. Stoeckl, M. Storm, T. C. Sangster, A. V. Maximov, and R. W. Short, Phys. Plasmas **14**, 056301 (2007).